# Toward Design of Synergistically Active Carbon-Based Catalysts for Electrocatalytic Hydrogen Evolution

Yao Zheng,[†,‡,||] Yan Jiao,[†,||] Lu Hua Li,[§] Tan Xing,[§] Ying Chen,[§] Mietek Jaroniec,[⊥] and Shi Zhang Qiao[†,*]

[†]School of Chemical Engineering, The University of Adelaide, Adelaide, South Australia 5005, Australia, [‡]Australian Institute for Bioengineering and Nanotechnology, University of Queensland, Brisbane, Queensland 4072, Australia, [§]Institute for Frontier Materials, Deakin University, Waurn Ponds, Victoria 3216, Australia, and [⊥]Department of Chemistry and Biochemistry, Kent State University, Kent, Ohio 44240, United States. [||]These authors contributed equally to this work.

ABSTRACT Replacement of precious Pt catalyst with cost-effective alternatives would be significantly beneficial for hydrogen production *via* electrocatalytic hydrogen evolution reaction (HER). All candidates thus far are exclusively metallic catalysts, which suffer inherent corrosion and oxidation susceptibility during acidic proton-exchange membrane electrolysis. Herein, based on theoretical predictions, we designed and synthesized nitrogen (N) and phosphorus (P) dual-doped graphene as a nonmetallic electrocatalyst for sustainable and efficient hydrogen production. The N and P heteroatoms could coactivate the adjacent C atom in the graphene matrix by affecting its valence orbital energy levels to induce a synergistically enhanced reactivity toward HER. As a result, the dual-doped graphene showed higher electrocatalytic HER activity than single-doped ones and comparable performance to some of the traditional metallic catalysts.
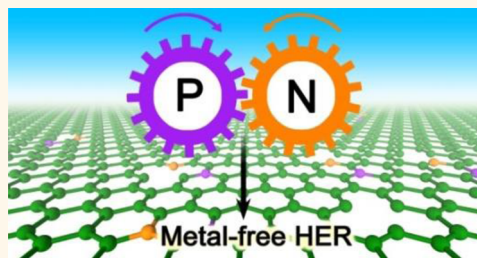
KEYWORDS: dual-doped graphene · synergistic catalysis · hydrogen evolution · metal-free catalysis · theoretical prediction

E lectrocatalytic reduction of water to molecular hydrogen *via* hydrogen evolution reaction (HER) provides a promising solution to energy supplies in the future. The corresponding devices always require noble metal catalysts, such as Pt, to facilitate low overpotential and fast kinetics for practical applications.[1,2] However, the high cost as well as low abundance of Pt limit their widespread use. Therefore, replacement of noble metals with cost-effective but highly efficient alternatives is desirable to achieve large-scale energy production. In recent years, a wide variety of transition metals (Co, Ni, Fe, Mo) and derivative components have been selected as effective candidates; however, the inherent corrosion and oxidation susceptibility largely limits their utilization in acidic proton-exchange membrane-based electrolysis for sustainable hydrogen production.[3−9] On the other hand, various carbon-based materials feature unique advantages for designated catalysis due to their tunable molecular structures, abundance, and strong tolerance to acidic/alkaline environments. Very recent advances in low-dimensional carbon materials,

as metal-free catalysts, have shown their promising future in energy-related electrocatalytic oxygen reduction/evolution reactions (ORR/OER).

In the case of ORR, we have found that some carbon-based catalysts showed comparable electrocatalytic activity with that of precious Pt and further possessed enhanced stability and fuel tolerance, which make them as competitive alternatives to Pt.[10,11] Generally, the engineering of pristine graphene by chemical substitution of some carbon atoms with heteroatoms, such as N, B, P, F, and S, is an effective way to tailor its electronic structure and (electro)chemical properties.[12−17] In particular, the codoping of two elements with reverse electronegativity to that of carbon, *e.g.*, B and N, could lead to a unique electron-donor property of carbon by the so-called synergistic coupling effect between two heteroatoms and, consequently, largely boost its ORR activity.[10,11] However, current knowledge about electrocatalytic HER on graphene surface is very inconclusive, and the systemic catalysts' molecular design toward dual-doped graphenes for highly efficient HER is still lacking.
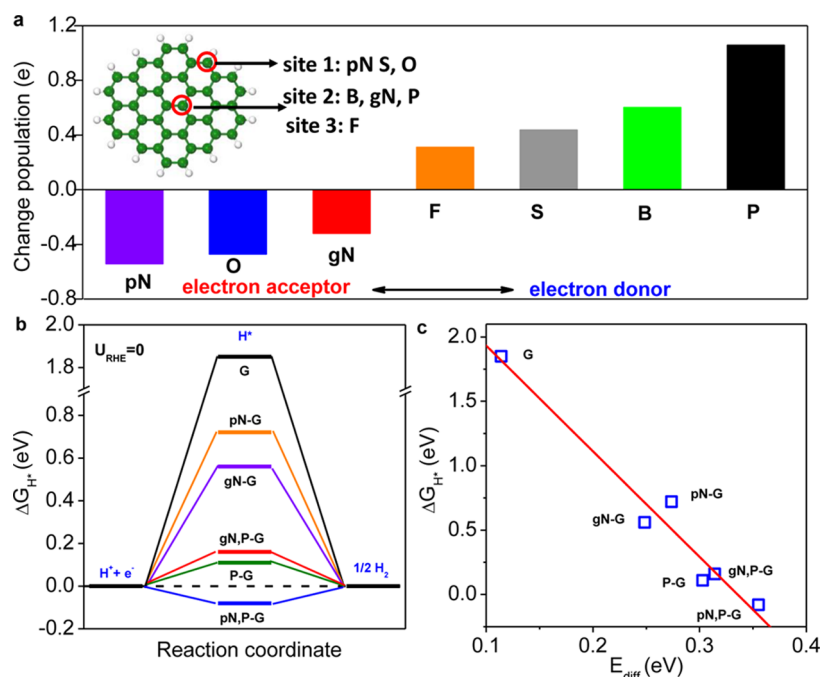
Figure 1. (a) NBO population analysis of six different nonmetallic heteroatoms in graphene matrix. pN and gN represent pyridinic and graphitic type of N, respectively. Inset shows the proposed doping sites for different elements, sites 1 and 2 are the edge and center in-plane sites, respectively, and site 3 is an out-of-plane center site in graphene. (b) The calculated free energy (ΔG_{H*}) diagram for HER at the equilibrium potential ($U_{RHE} = 0$ V) for N- and/or P-doped graphene models. (c) Relationship between ΔG_{H*} and E_{diff} for various models.

Although graphene-based materials have been extensively studied in electrochemical applications such as fuel cells, supercapacitors, and Li batteries,[18] there are few reports about their application in electrocatalytic hydrogen production, and more importantly, no theoretical calculations have been performed to predict their unexplored electrocatalytic capacities in relation to this key energy conversion process.[19]

Herein, we present our attempt to design a dual-doped graphene catalyst with a synergistically enhanced HER activity to extend the electrochemical applications of graphene materials. First, we used density functional theory (DFT) calculations to explore several nonmetallic element-doped graphene models, followed by selecting one couple of heteroatoms (N and P) as codopants with remarkable contrast in their charge population in graphene matrix. By downshifting the valence bands of active carbons in graphene, the codoping of N and P indeed resulted in the highest HER activity among various doped graphene models. On the basis of the theoretical prediction, the proof-of-concept studies were carried out by simultaneously incorporating N and P heteroatoms into the graphene matrix through a typical chemical-doping procedure. The resultant N,P-graphene catalyst showed much lower HER overpotential and higher exchange current density than those of all investigated pure and doped graphene samples. The newly developed nonmetallic catalyst also showed robust stability and applicability in a wide range of pH values. These findings provide solid evidence, both

theoretical and experimental, that similar to precious metals, the well-designed carbon-based counterparts also have a great potential as highly efficient HER catalysts.

RESULTS AND DISCUSSION

To explore the effects of various dopants in graphene toward HER activity, we carried out systematic studies on the electronic properties of differently doped graphene models by DFT calculations. We selected six nonmetallic heteroatoms (N, B, O, S, P, F) with various electron negativities to investigate their effects on the adjacent C atoms, which act as the active sites for HER (Supporting Information, Figure S1). All the proposed doping configurations were constructed on the basis of the reported experimental X-ray photoelectron spectra (XPS) data by taking into account the chemical environment of each heteroatom.[20] The natural bond orbital (NBO) population analyses (Figure 1a) show that six dopants possess various charge populations in graphene matrix: N and O are negatively charged (act as electron acceptors for the adjacent C), while F, S, B, and P are positively charged (act as electron donors). Therefore, we selected one couple of the investigated atoms with the most noticeable differences in the charge population (*i.e.*, N and P) as codopants for graphene to maximally activate the adjacent C atom by tailoring its electron donor–acceptor property and consequently enhance its HER activity.

The HER activities of a series of the proposed N- and/or P-doped graphene clusters were then theoretically

predicted by the HER free energy diagram (Figure 1b). Generally, the overall HER pathway, simply written as $2H^+ + 2e^- \rightarrow H_2$, can be described by a three-state diagram comprising of an initial state $H^+ + e^-$, an intermediate adsorbed H*, and the final product $^1/_2 H_2$. The Gibbs free-energy of the hydrogen adsorption, $|\Delta G_{H^*}|$, has been considered as the major descriptor of the HER activity for a wide variety of metal surfaces.[21,22] The optimal value of $|\Delta G_{H^*}|$ should be zero; if ΔG_{H^*} is positive, the formation of intermediate H* would be the rate-determining step (RDS) of the whole HER; while if ΔG_{H^*} is negative, desorption of H* to form H_2 is the RDS.[22] Among graphene-based models, pure graphene shows a highly positive ΔG_{H^*} value (1.85 eV), representing a negligible HER activity. Both N and/or P incorporation could reduce the ΔG_{H^*} values to enhance the initial H* adsorption, in which pyridinic N and P dual-doped model (pN,P-G) demonstrates the lowest $|\Delta G_{H^*}|$ value of 0.08 eV (Figure 1b and Supporting Information, Figure S2), indicating its highest HER activity with the most favorable H* adsorption−desorption property. In contrast to most of the single-doped graphenes which have a positive ΔG_{H^*} (Supporting Information, Figure S3), the negative ΔG_{H^*} of the dual-doped pN,P-G indicates a relatively strong H* adsorption on its surface; for such a model, the C atom between *meta*-type pN and P in the heteroring acts as the most active site for H* adsorption (Supporting Information, Figure S4).

We further explored the origin of the different H* adsorption behavior on these doped graphenes using the molecular orbital theory.[23] As shown in Figure 1c, the ΔG_{H^*} values of all investigated models show a linear trend in relation to E_{diff} (E_{diff} is defined as the difference between the lowest valence orbital energy of C active center and the highest valence orbital energy of the graphene cluster). The principle underlying this relationship is that the valence band (v) of the active C atom hybridizes with the bonding (σ) orbital of the adsorbed H* to form bonding (v-σ) and antibonding (v-σ)* states, as illustrated in the Supporting Information (Scheme S1). An increase in the filling of the (v−σ) state, as induced by lower C valence orbitals, could lead to a stronger bonding between H* and active C to reduce the ΔG_{H^*}. Among all investigated models, the pN,P-G cluster shows the highest value of E_{diff}, which corresponds to the lowest value of ΔG_{H^*} and apparently the highest predicted HER activity (Figure 1c).

To verify the theoretical predictions, we incorporated N and P in graphene simultaneously by annealing chemically exfoliated graphene oxide (GO) powder with a melamine (N source) and triphenylphosphine (P source) mixture at 950 °C in Ar atmosphere. During the reduction process of GO, N and P were chemically doped into the defective sites of graphene by substituting C or O atoms, yielding a doping concentration of 4.60 atom % of N and 1.63 atom % of P, respectively (based on the XPS results). As control samples, the
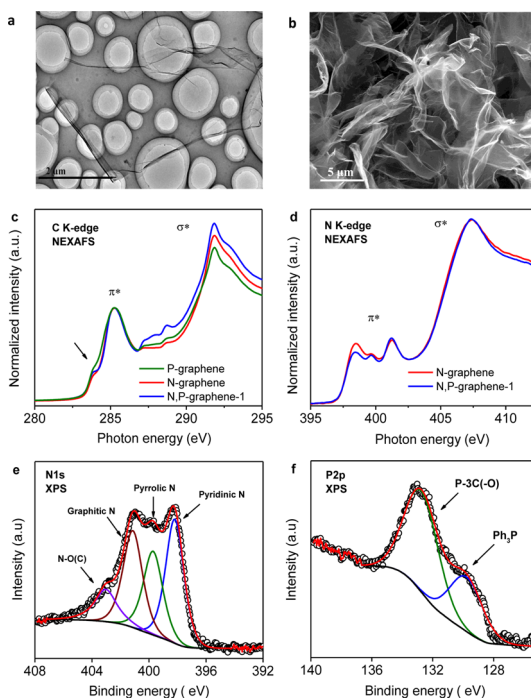

Figure 2. (a, b) TEM and SEM images of N,P-graphene-1 nanosheets. (c, d) C and N K-edge NEXAFS spectra of N- and/or P-doped graphenes. (e, f) N 1s and P 2p high resolution XPS spectra of N,P-graphene-1. In panel e, four nitrogen binding configurations represent pyridinic-, pyrrolic-, and graphitic-N species (B.E. = 398.2, 399.7, 401.2 eV) and oxidative N−O(−C) species (B.E. = 403.0 eV).[14] In panel f, two phosphorus binding configurations represent P−3C(−O) species (B.E. = 132.9 eV) in the basal plane of graphene and a small amount of P−C species (B.E. = 129.9 eV) remaining from precursor.[15]

single-doped N- or P-graphenes were respectively synthesized by the same procedure with addition of a single respective precursor (Supporting Information, Figure S5a,b). The nanosheet morphology of the pristine GO was well preserved in the resultant N,P-graphene-1 without noticeable residues of the solid precursors, as shown in the scanning electron microscope (SEM) and transmission electron microscopy (TEM) images (Figure 2a,b). The electron energy loss spectrum (EELS) elemental mapping shows a homogeneous distribution of the various dopants in the graphene matrix (Supporting Information, Figure S6). The nature of doping was first identified by near-edge X-ray adsorption fine structure spectroscopy (NEXAFS) as shown in Figure 2c,d. In the C K-edge (Figure 2c), all three N- and/or P-doped samples exhibited typical graphitic-sp^2 carbon structures with strong π^* and σ^* resonances at ~285.5 and ~292.0 eV, representing the core level electron transitions to the unoccupied antibonding π^* and σ^* orbitals, respectively. The successful N incorporation was revealed by the N K-edge NEXAFS spectra (Figure 2d), showing three π^* resonances representing N−C bonds in the form of pyridine (398.5 eV), pyrrole (399.7 eV), and graphite (401.2 eV) structures, respectively, also consistent with the XPS

results (Figure 2e).[14] Because the π^* resonances of C—C and C—P species have an overlapping position in the C K-edge NEXAFS (only a weak shoulder at ~283.2 eV that can be attributed to the π^*_{C-P} resonance in P-containing N,P-graphene-1 and P-graphene samples but not N-graphene, as shown by the arrow in Figure 2c), the doping of P in N,P-graphene-1 was confirmed by Synchrotron-based high-resolution XPS (Figure 2f), indicating that P heteroatom is mainly bonded to C or O atoms, along with some Ph_3P precursor residue.[15] Note that both NEXAFS and XPS spectra indicate that N and P heteroatoms were not bonded to each other to form any P—N species (i.e., phosphorus nitride, P_3N_5) in or out of the graphene basal plane which was predicted has worst HER activity than meta and para site P—C—N moieties (Supporting Information, Figure S4).

The electrocatalytic activities of the as-synthesized N- and/or P-doped graphenes toward HER were examined in both acidic (0.5 M H_2SO_4) and alkaline (0.1 M KOH) aqueous solutions. Figure 3a shows the HER polarization curves of various electrocatalysts in 0.5 M H_2SO_4 solution. Graphite (as the example of pure graphene without any heteroatom doping) had a negligible electrocatalytic activity, while either single N or P doping could significantly enhance the HER activity of graphene by generating additional active sites, which is consistent with theoretical prediction (Figure 1b). To achieve a 10 mA/cm^2 HER current density, the dual-doped N,P-graphene-1 required an overpotential of ~420 mV, lower than those of both single-doped N and P-graphenes (Supporting Information, Table S1). It should be noted that the HER activity of the N,P-graphene-1 is comparable to that of some traditional metallic catalysts, such as bulk Au, Mo and Mo/Ni alloy, etc.,[24−26] while it is not as good as that of the state-of-the-art nanostructured MoS_2/WS_2 and Ni—Mo alloy catalysts. This may be due to the bulk nature and the lack of a large population of active sites because of the stacking graphene layers during the N,P-graphene-1 electrode preparation (drying) process. Both of these factors result in a relatively lower electrochemically active surface area on N,P-graphene-1 than other nanostructured catalysts. However, the comparable normalized HER exchange current densities of N,P-graphene-1 and the well-studied metallic catalysts (nanostructured MoS_2 for example,[7,27−30] see Figure S7 and Table S2 in the Supporting Information for detailed normalization procedure) indicate that the graphene-based materials have the potential to achieve comparable activity to the metallic catalysts via nanostructure engineering/optimizing.

The electrocatalytic activity enhancement in the case of N,P-graphene-1 as compared to single-doped samples could be fundamentally revealed by exploring their HER mechanisms. As shown in Figure 3b, all N- and/or P-doped graphenes showed Tafel slopes in a
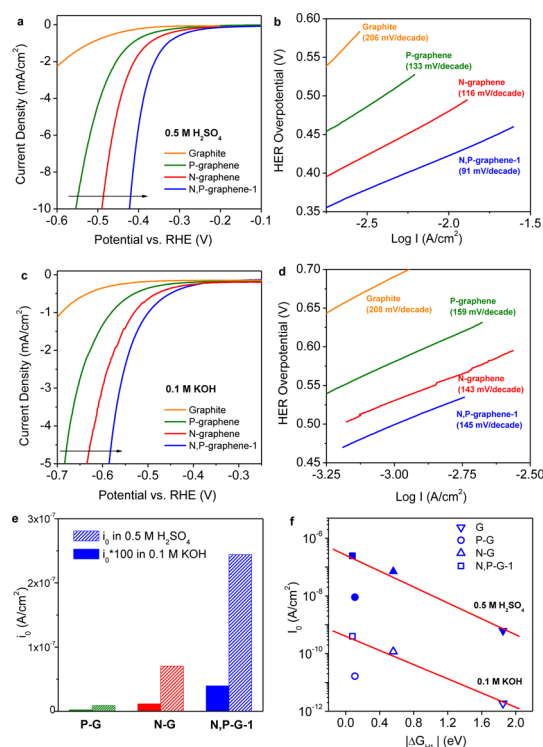

Figure 3. HER polarization curves and the corresponding Tafel plots of N- and/or P-doped graphene electrocatalysts in (a, b) 0.5 M H_2SO_4 (pH = 0) and (c, d) 0.1 M KOH (pH = 13). (e) Comparison of calculated i_0 values for N- and/or P-doped graphenes in 0.5 M H_2SO_4 (patterned bars) and 0.1 M KOH (solid bars) solutions. (f) Relationships between i_0 and ΔG_{H^*} for N- and/or P-doped graphenes.

range of ~90 to ~130 mV/decade (N,P-graphene-1 possessed the lowest value of 91 mV/decade), indicating that an initial proton adsorption (i.e., Volmer step: $H^+ + e^- \rightarrow H^*$) was the rate-determining step of the whole HER process.[3] These behaviors could be theoretically explained by thermodynamic calculations (Figure 1b and Supporting Information, Figure S3), in which almost all investigated graphene-based catalysts demonstrate positive ΔG_{H^*} values related to a weak H* adsorption.[22] On the contrary, the N,P-graphene model shows a slightly negative ΔG_{H^*} with an enhanced capability to adsorb hydrogen which therefore can accelerate the most sluggish step (H* adsorption) of the whole HER process. As the result, a higher HER activity was experimentally observed.

In contrast to traditional metallic and the state-of-the-art nanostructured MoS_2 electrocatalysts, which are active under either acidic or basic conditions,[4,31,32] the newly developed graphene-based catalysts showed favorable HER activity in a wide range of pH values. As expected, in alkaline solution, the HER activities of all four graphene-based electrocatalysts were lower than those in acidic solutions but the activity followed the same trend (Figure 3c). The difference may arise from the different HER mechanism under the two conditions,[33] e.g., there is an additional water dissociation step in the alkaline solution and graphene-based catalysts is unfavorable to

facilitate this step therefore resulting in a relative high energy barrier in the whole HER process.

The synergistic coupling effect in N,P-graphene-1 was quantitatively evaluated in terms of the exchange current density (i_0) derived from the Tafel plots. As summarized in Figure 3e, the dual-doped N,P-graphene-1 showed $i_0 = 2.4 \times 10^{-7}$ A/cm^2 and 4.0×10^{-10} A/cm^2 in acidic and alkaline solutions, which surpassed the summed value of single doped N-graphene and P-graphene in respective solutions (Supporting Information, Table S1). Such a difference indicates that the enhanced electrocatalytic activity of N,P-graphene-1 is not caused by a simple increase in the number of active sites by codoping N and P heteroatoms but represents the synergistic effect that boost the capacity of proton adsorption and reduction, as revealed by the aforementioned DFT calculations. To gain more insight into the relationship between the apparent HER performance and the theoretical activity descriptor for newly developed carbon-based catalysts, the experimentally measured i_0 was correlated with the DFT-derived ΔG_{H*}, which is commonly used in the study of metal surfaces.[21] As shown in Figure 3f, a good linear trend between the theoretical and experimental values is clearly visible (excluding P-graphene), which also validates the predictive capability of the employed DFT model beyond metals.[21] Regarding P-graphene, different from the cases of other three catalysts, the sample was highly hydrophobic hence the mass transport limitation might be the major contributor for its poor HER activity.

One of significant features of carbon materials is their strong tolerance to both acidic and alkaline solution. As expected, the N,P-graphene-1 catalyst with strong covalent C—N and C—P bonds featured a robust stability in both 0.5 M H$_2$SO$_4$ and 0.1 M KOH solutions without corrosion and oxidation, which is required for a sustainable hydrogen production (Figure 4a). As a control sample, two-step synthesized N,P-graphene-2 (see the Experimental Section for a detailed synthesizing procedure) showed lower HER activity than that of one-step synthesized N,P-graphene-1 (Figure 4b), due to the different N and P doping concentrations (Supporting Information, Figure S5c,d). Also note that not each graphene codoped by a random couple of heteroatoms could achieve an enhanced HER activity. As shown in Figure 4b, the boron- and nitrogen-codoped graphene (B,N-graphene), which has demonstrated a synergistic catalysis toward electrocatalytic ORR activity enhancement,[10] unexpectedly showed lower
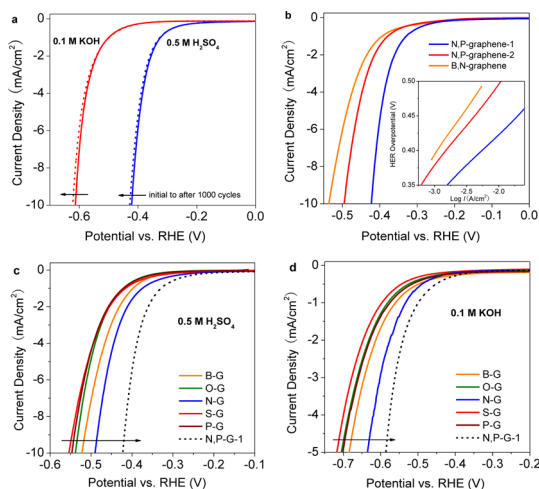

Figure 4. (a) Polarization curves of N,P-graphene-1 recorded before and after 1000 potential sweeps (+0.2 to −0.6 V vs RHE) in acidic and alkaline solutions, respectively. (b) Comparison of the polarization curves and Tafel plots (inset) of one-step synthesized N,P-graphene-1 versus two-step synthesized N,P-graphene-2 as well as B,N-graphene[10] in 0.5 M H$_2$SO$_4$ solution. (c, d) HER polarization curves of different single-doped graphene catalysts as compared to that of dual-doped graphene in both acid and base solutions.

HER activity than that of single-doped N-graphene and N,P-graphene-1. These experimental findings indicate the N/P dual doping is crucial for the favorable HER activity in the case of N,P-graphene-1. Additionally, the dual-doped graphene electrocatalysts showed higher HER activity than all of investigated single-doped ones (N-, B-, O-, S-, P-doped graphenes) in both acidic and alkaline solutions (Figure 4c,d), unambiguously indicating that the synergistic effect of dual doping in N,P-graphene-1 led to its enhanced electrocatalytic activity.

CONCLUSIONS

In summary, based on the DFT-calculations, we designed and synthesized N and P dual-doped graphene as a metal-free catalyst for electrocatalytic HER, which exhibited a significantly improved electrochemical performance as compared to single doped counterparts due to the synergistic effect confirmed by both electrochemical measurements and theoretical calculations. By applying HER as a test reaction, which is also considered as a cornerstone to explore the mechanism of other multielectron transfer processes,[6] we expect that this study will largely expand the spectrum of catalysts for other energy-related electrocatalytic reactions.

EXPERIMENTAL SECTION

Computational Screening Procedure. The explored graphene models (as shown in Supporting Information, Figure S1) are based on C$_{42}$H$_{16}$ clusters which have been previously adopted for investigation of ORR on boron and nitrogen doped graphene.[10]

The geometry optimizations of these molecular models were carried out using density functional theory (DFT) calculations provided by Gaussian 09.[34] All the calculations were performed at UB3LYP/6-31G(d,p) level of chemistry with all atoms fully relaxed. The solvent (water) effect was considered by the Polarizable

Continuum Model (PCM).[35] The charge population was calculated by NBO analysis.[23] During our investigation, only the intermediate states in the HER process (*i.e.*, H* adsorption), as well as the reactant (*i.e.*, Graphene + H$^+$) and product state (*i.e.*, graphene + $^1/_2$H$_2$, set as the reference level for free energy), were proposed and evaluated; extra energy barriers might exist but were not considered due to the unbalanced electron numbers beared by different states. The free energy of H* adsorption for various catalyst models is the criterium to evaluate catalysts' HER activities.[21] Within each model, the heteroatom themselves, as well as several carbon atoms around the dopants, were investigated regarding to the corresponding ΔG_{H*}, and the one with the lowest ΔG_{H*} is presented in the Results and Discussion.

Materials Synthesis. Pristine GO was prepared from graphite flakes using a slightly modified Hummers' method. The GO powder was collected by lyophilization for further doping procedure. N-graphene and P-graphene were respectively prepared by mixing an initial GO powder with melamine (C$_3$H$_6$N$_6$) or triphenylphosphine ((C$_6$H$_5$)$_3$P) at a mass ratio of 1:10. Then the mixture was annealed in Ar up to 950 °C for 3 h with a heating rate of 3 °C/min. Two recipes were used to prepare N,P-graphene either by direct annealing of mixed melamine and triphenylphosphine with an initial GO powder (mass ratio is 10:10:1) in Ar at 950 °C for 3 h (single-step, the product is named as N,P-graphene-1) or by a two-step process involving (1) preparation of P-graphene and (2) incorporation of N- into P-graphene to form N,P-graphene-2. Note that in the case of two-step step process, a reverse sequence that involves at first the incorporation of N followed by introduction of P do not produce the codoped graphene because it is difficult to incorporate P into the N-graphene matrix in the second step.

Chemical Characterization. The near-edge X-ray adsorption fine structure (NEXAFS) measurements were carried out in an ultrahigh vacuum chamber ($\sim$10^{-10} mbar) of the undulator soft X-ray spectroscopy beamline at the Australian Synchrotron. The TEY yield was recorded using a microchannel plate detector. In both carbon and nitrogen K-edge region scans, 50 meV energy steps were used. The raw NEXAFS data were normalized to the photoelectron current of the photon beam, measured on an Au grid. The synchrotron-based X-ray photoelectron spectra (XPS) were collected by a high-resolution and high-sensitivity hemispherical electron analyzer with nine channel electron multipliers (SPECS Phoibos 150). In the survey scans, the excitation energy was 1486.7 eV. In the high-resolution scans, the excitation energy was 700 eV for a better signal-to-noise ratio and the E-pass was set to 5 eV for optimum energy resolution. The excitation photon energies were calibrated by the photon energy measured on a reference Au sample and the binding energies were normalized by the C–C peak at 284.5 eV. The Scanning electron microscope (SEM) images were taken with Philips XL30 FEG SEM. The Transmission electron microscopy (TEM) and electron energy-loss spectrum (EELS) mapping were obtained using a JEOL 2100F machine operated at 200 kV and equipped with a Gatan GIF Quantum.

Electrode Preparation and Electrochemical Characterization. Taking N,P-graphene-1 electrode as an example, the catalyst was ultrasonically dispersed in distilled water (Milli-Q) containing 0.1 wt % of Nafion. An aqueous dispersion of the catalyst (40 μL, 1.0 mg/mL) was then transferred onto the glassy carbon rotating disk electrode (RDE, 0.196 cm^2, Pine Research Instrumentation, Durham, NC) serving as a working electrode. The reference electrode was an Ag/AgCl in 4 M AgCl–KCl solution. All potentials were referenced to a reversible hydrogen electrode (RHE) by adding a value of (0.205 + 0.059 × pH) V, and all polarization curves were corrected for the *i*R contribution within the cell. A flow of N$_2$ was maintained over the electrolyte during the experiment to eliminate dissolved oxygen. The working electrode was rotated at 1600 rpm to remove hydrogen gas bubbles formed at the catalyst surface.

Conflict of Interest: The authors declare no competing financial interest.

Supporting Information Available: Molecular structures and hydrogen adsorption configuration of different investigated models. The scheme of orbital hybridization of valence band for HER active sites and H* bonding orbital. More details of chemical and electrochemical characterization. A detailed normalization procedure of the exchange current density of N,P-graphene catalyst. This material is available free of charge *via* the Internet at http://pubs.acs.org.

REFERENCES AND NOTES

1. Lewis, N. S.; Nocera, D. G. Powering the Planet: Chemical Challenges in Solar Energy Utilization. *Proc. Natl. Acad. Sci. U.S.A.* **2001**, *103*, 15729–15735.

2. Walter, M. G.; Warren, E. L.; McKone, J. R.; Boettcher, S. W.; Mi, Q.; Santori, E. A.; Lewis, N. S. Solar Water Splitting Cells. *Chem. Rev.* **2010**, *110*, 6446–6473.

3. Conway, B. E.; Tilak, B. V. Interfacial Processes Involving Electrocatalytic Evolution and Oxidation of H$_2$, and the Role of Chemisorbed H. *Electrochim. Acta* **2002**, *47*, 3571–3594.

4. Cook, T. R.; Dogutan, D. K.; Reece, S. Y.; Surendranath, Y.; Teets, T. S.; Nocera, D. G. Solar Energy Supply and Storage for the Legacy and Nonlegacy Worlds. *Chem. Rev.* **2010**, *110*, 6474–6502.

5. Zhuo, J.; Wang, T.; Zhang, G.; Liu, L.; Gan, L.; Li, M. Salts of C$_{60}$(OH)$_8$ Electrodeposited Onto a Glassy Carbon Electrode: Surprising Catalytic Performance in the Hydrogen Evolution Reaction. *Angew. Chem., Int. Ed.* **2013**, *52*, 10867–10870.

6. Jaramillo, T. F.; Jørgensen, K. P.; Bonde, J.; Nielsen, J. H.; Horch, S.; Chorkendorff, I. Identification of Active Edge Sites for Electrochemical H$_2$ Evolution From MoS$_2$ Nanocatalysts. *Science* **2007**, *317*, 100–102.

7. Kibsgaard, J.; Chen, Z.; Reinecke, B. N.; Jaramillo, T. F. Engineering the Surface Structure of MoS$_2$ to Preferentially Expose Active Edge Sites for Electrocatalysis. *Nat. Mater.* **2012**, *11*, 963–969.

8. Lukowski, M. A.; Daniel, A. S.; Meng, F.; Forticaux, A.; Li, L.; Jin, S. Enhanced Hydrogen Evolution Catalysis from Chemically Exfoliated Metallic MoS$_2$ Nanosheets. *J. Am. Chem. Soc.* **2013**, *135*, 10274–10277.

9. Xu, Y.; Gao, M.; Zheng, Y.; Jiang, J.; Yu, S. H. Nickel/Nickel(II) Oxide Nanoparticles Anchored onto Cobalt(IV) Diselenide Nanobelts for the Electrochemical Production of Hydrogen. *Angew. Chem., Int. Ed.* **2013**, *52*, 8546–8550.

10. Zheng, Y.; Jiao, Y.; Ge, L.; Jaroniec, M.; Qiao, S. Z. Two-Step Boron and Nitrogen Doping in Graphene for An Enhanced Synergistic Catalysis. *Angew. Chem., Int. Ed.* **2013**, *52*, 3110–3116.

11. Liang, J.; Jiao, Y.; Jaroniec, M.; Qiao, S. Z. Sulfur and Nitrogen Dual-Doped Mesoporous Graphene Electrocatalyst for Oxygen Reduction with Synergistically Enhanced Performances. *Angew. Chem., Int. Ed.* **2012**, *51*, 11496–11500.

12. Sun, X.; Song, P.; Zhang, Y.; Liu, C.; Xu, W.; Xing, W. A Class of High Performance Metal-Free Oxygen Reduction Electrocatalysts Based on Cheap Carbon Blacks. *Sci. Rep.* **2013**, *3*, 2505.

13. Liu, Z.-W.; Peng, F.; Wang, H.-J.; Yu, H.; Zheng, W.; Yang, J. Phosphorus-Doped Graphite Layers with High Electrocatalytic Activity for the O$_2$ Reduction in An Alkaline Medium. *Angew. Chem., Int. Ed.* **2011**, *50*, 3257–3261.

14. Raymundo-Pinero, E.; Cazorla-Amoros, D.; Linares-Solano, A.; Find, J.; Wild, U.; Schlogl, R. Structural Characterization of N-Containing Activated Carbon Fibers Prepared from A Low Softening Point Petroleum Pitch and A Melamine Resin. *Carbon* **2002**, *40*, 597–608.

15. Liu, Z.; Peng, F.; Wang, H.; Yu, H.; Tan, J.; Zhu, L. Novel Phosphorus-Doped Multiwalled Nanotubes with High Electrocatalytic Activity for O$_2$ Reduction in Alkaline Medium. *Catal. Commun.* **2011**, *16*, 35–38.

16. Lee, W. H.; Suk, J. W.; Chou, H.; Lee, J. S.; Hao, Y.; Wu, Y.; Piner, R.; Akinwande, D.; Kim, K.; Ruoff, R. S. Selective-Area Fluorination of Graphene with Fluoropolymer and Laser Irradiation. *Nano Lett.* **2012**, *12*, 2374–2378.

17. Geng, D.; Chen, Y.; Chen, Y.; Li, Y.; Li, R.; Sun, X.; Ye, S.; Knights, S. High Oxygen-Reduction Activity and Durability of Nitrogen-Doped Graphene. *Energy Environ. Sci.* **2011**, *4*, 760–764.

18. Sun, Y.; Wu, Q.; Shi, G. Graphene Based New Energy Materials. *Energy Environ. Sci.* **2011**, *4*, 1113–1132.

19. Zheng, Y.; Jiao, Y.; Zhu, Y.; Li, L. H.; Han, Y.; Chen, Y.; Du, A.; Jaroniec, M.; Qiao, S. Z. Hydrogen Evolution by A Metal-Free Electrocatalyst. *Nat. Commun.* **2014**, *5*, 3783.

20. Jiao, Y.; Zheng, Y.; Jaroniec, M.; Qiao, S. Z. Origin of the Electrocatalytic Oxygen Reduction Activity of Graphene-Based Catalysts: A Roadmap to Achieve the Best Performance. *J. Am. Chem. Soc.* **2014**, *136*, 4394–4403.

21. Nørskov, J. K.; Bligaard, T.; Logadottir, A.; Kitchin, J. R.; Chen, J. G.; Pandelov, S.; Stimming, U. Trends In the Exchange Current for Hydrogen Evolution. *J. Electrochem. Soc.* **2005**, *152*, J23–J26.

22. Greeley, J.; Jaramillo, T. F.; Bonde, J.; Chorkendorff, I.; Nørskov, J. K. Computational High-Throughput Screening of Electrocatalytic Materials for Hydrogen Evolution. *Nat. Mater.* **2006**, *5*, 909–913.

23. Reed, A. E.; Weinhold, F. Natural Bond Orbital Analysis of Near-Hartree-Fock Water Dimer. *J. Chem. Phys.* **1983**, *78*, 4066–4073.

24. Chen, W.-F.; Sasaki, K.; Ma, C.; Frenkel, A. I.; Marinkovic, N.; Muckerman, J. T.; Zhu, Y.; Adzic, R. R. Hydrogen-Evolution Catalysts Based on Non-Noble Metal Nickel Molybdenum Nitride Nanosheets. *Angew. Chem., Int. Ed.* **2012**, *51*, 6131–6135.

25. Chen, W.-F.; Wang, C.-H.; Sasaki, K.; Marinkovic, N.; Xu, W.; Muckerman, J. T.; Zhu, Y.; Adzic, R. R. Highly Active and Durable Nanostructured Molybdenum Carbide Electrocatalysts for Hydrogen Production. *Energy Environ. Sci.* **2013**, *6*, 943–951.

26. Perez, J.; Gonzalez, E. R.; Villullas, H. M. Hydrogen Evolution Reaction on Gold Single-Crystal Electrodes in Acid Solutions. *J. Phys. Chem. B* **1998**, *102*, 10931–10935.

27. Xie, J.; Zhang, J.; Li, S.; Grote, F.; Zhang, X.; Zhang, H.; Wang, R.; Lei, Y.; Pan, B.; Xie, Y. Controllable Disorder Engineering in Oxygen-Incorporated MoS_2 Ultrathin Nanosheets for Efficient Hydrogen Evolution. *J. Am. Chem. Soc.* **2013**, *135*, 17881–17888.

28. Liao, L.; Zhu, J.; Bian, X.; Zhu, L.; Scanlon, M.; Girault, H.; Liu, B. MoS_2 Formed on Mesoporous Graphene As a Highly Active Catalyst for Hydrogen Evolution. *Adv. Funct. Mater.* **2013**, *23*, 5326–5333.

29. Merki, D.; Vrubel, H.; Rovelli, L.; Fierro, S.; Hu, X. Fe, Co, and Ni Ions Promote the Catalytic Activity of Amorphous Molybdenum Sulfide Films for Hydrogen Evolution. *Chem. Sci.* **2012**, *3*, 2515–2525.

30. Chen, Z.; Cummina, D.; Reinecke, B.; Clark, E.; Sunkara, M.; Jaramillo, T. Core-Shell MoO_3-MoS_2 Nanowires for Hydrogen Evolution: A Functional Design for Electrocatalytic Materials. *Nano Lett.* **2011**, *11*, 4168–4175.

31. Popczun, E. J.; McKone, J. R.; Read, C. G.; Biacchi, A. J.; Wiltrout, A. M.; Lewis, N. S.; Schaak, R. E. Nanostructured Nickel Phosphide As an Electrocatalyst for the Hydrogen Evolution Reaction. *J. Am. Chem. Soc.* **2013**, *135*, 9267–9270.

32. McKone, J. R.; Sadtler, B. F.; Werlang, C. A.; Lewis, N. S.; Gray, H. B. Ni-Mo Nanopowders for Efficient Electrochemical Hydrogen Evolution. *ACS Catal.* **2013**, *3*, 166–169.

33. Durst, J.; Siebel, A.; Simon, C.; Hasche, F.; Herranz, J.; Gasteiger, H. A. New Insights Into the Electrochemical Hydrogen Oxidation and Evolution Reaction Mechanism. *Energy Environ. Sci.* **2014**, 10.1039/C4EE00440J.

34. Frisch, M. J.; Trucks, G. W.; Schlegel, H. B.; Scuseria, G. E.; Robb, M. A.; Cheeseman, J. R.; Scalmani, G.; Barone, V.; Mennucci, B.; Petersson, G. A. et al. *Gaussian09* (Revision A.02); Gaussian: Wallingford, CT, 2009.

35. Tomasi, J.; Mennucci, B.; Cammi, R. Quantum Mechanical Continuum Solvation Models. *Chem. Rev.* **2013**, *105*, 2999–3093.